electricity

Article

# Novel Current-Fed Bidirectional DC-DC Converter for Battery Charging in Electric Vehicle Applications with Reduced Spikes

**Piyush Sharma [1], Dheeraj Kumar Palwalia [1], Ashok Kumar Sharma [1], Yatindra Gopal [2,*]**
**and Julio C. Rosas-Caro [3,*]**

[1] Department of Electrical Engineering, Rajasthan Technical University, Kota 324010, India; piyushsharma034@gmail.com (P.S.); dkpalwalia@rtu.ac.in (D.K.P.); aksharma@rtu.ac.in (A.K.S.)
[2] Department of Electrical and Electronics Engineering, Lendi Institute of Engineering & Technology, Vizianagaram 535005, India
[3] Facultad de Ingenieria, Universidad Panamericana, Alvaro del Portillo 49, Zapopan 45010, Mexico
* Correspondence: ygopal.phd@rtu.ac.in (Y.G.); crosas@up.edu.mx (J.C.R.-C.)

**Abstract:** Electric vehicles (EVs) have emerged as the best alternative to conventional fossil fuel-based vehicles due to their lower emission rate and operating cost. The escalating growth of EVs has increased the necessity for distributed charging stations. On the other hand, the fast charging of EVs can be improved by the use of efficient converters. Hence, the fractional order proportional resonant (FOPR) controller-based current-fed bidirectional DC-DC converter is proposed in this work for EV charging applications. The output capacitance of the switches is utilized to achieve the resonance condition for zero voltage switching (ZVS) and zero current switching (ZCS). The proposed converter topology is implemented using the MATLAB Simulink tool. The result analysis verified that the proposed converter topology provides better switching characteristics for different operating modes, which is necessary for a high-voltage EV charger. Hence, it is proved that the proposed converter is more efficient for battery charging in EVs.

**Keywords:** current-fed dual active bridge; FOPR controller; ZVS; phase shift; pulse width modulation

check for updates

**Citation:** Sharma, P.; Palwalia, D.K.; Sharma, A.K.; Gopal, Y.; Rosas-Caro, J.C. Novel Current-Fed Bidirectional DC-DC Converter for Battery Charging in Electric Vehicle Applications with Reduced Spikes. *Electricity* **2024**, *5*, 1022–1048. https://doi.org/10.3390/electricity5040052

Academic Editors: Andreas Sumper and Pedro Manuel Soares Moura

Received: 31 August 2024
Revised: 4 December 2024
Accepted: 6 December 2024
Published: 13 December 2024

## 1. Introduction

The power electronic converter is a device that converts power from one form to another by changing the voltage levels. Based on the type of conversion, the converters are categorized into AC-DC, DC-DC, AC-AC, and DC-AC converters, which are used in renewable energy conversion, electric vehicles, industrial automation, and consumer electronics. [1]. DC-DC converters are extensively used in modern electronic systems to transfer power from the source to the load [2]. The isolated DC-DC converters meet multiple power conversion applications' input and output requirements [3]. The bidirectional converters are gaining more attention due to the advantage of power conversion in both directions. The bidirectional converter is widely used in EV charging applications due to its ability to power conversion between the grid and EVs. The existing bidirectional DC-DC converter is characterized as voltage-fed or current-fed [4]. The unidirectional and bidirectional converters are used in EV charging applications to charge the EV batteries. In a buck converter, the output voltage is lower than the input voltage, whereas the output voltage is higher than the input voltage in the boost converter [5].

Furthermore, the converters are categorized into voltage-fed and current-fed converters depending on the input source. The voltage-fed converters require a high winding ratio between the primary and secondary sides of the transformer to enhance the boosting action, which causes system complexities like higher voltage spikes across the switches [6,7]. The voltage-fed converters are affected by shoot-through problems. The current-fed DC-DC converter minimizes input current ripples [8]. Due to the improved short circuit protection, the current-fed power converters are used in lower and higher current meritorious applications [9]. The current-fed converters minimize the input filter requirement and higher voltage gains [10]. Furthermore, the current-fed topology reduces the switches' conduction losses and current rating [11]. The soft switching operation is the major requirement of the converter topology, which includes ZVS and ZCS that is achieved by proper converter modeling, which improves the system efficiency [12,13].

In recent power generation technologies, batteries have been used for power storage and power transmission applications [14]. The battery charging application needs an efficient converter to cope with the charging and discharging behavior of the battery. The converter design for battery application must consider some necessary aspects like current ripple, voltage ripple, and voltage variations [15]. Thus, due to their high power density, current-fed bidirectional DC-DC converters are used in battery applications [16]. The bidirectional DC-DC converters control the power flowing from the energy storing devices [17]. The current-fed three-port DC-DC converters are employed in battery charging applications due to their efficacy in performance [18]. The current-fed double inductor push–pull converter is used in the current charger for higher-voltage capacitors [19]. Due to the multiport interface's ability, the current-fed dual active bridge DC-DC converters are used in energy storage systems [20].

Moreover, an improved charging mechanism was introduced in [21], which suggested that the model ensures high-power quality under different power supply modes. The high-power charging and its control mechanism are suggested in [22]. In advance, multi-agent systems [23,24] are used in microgrid. Various converter configurations are discussed in [25] to assess their performance under EV operation. By analyzing existing works in the literature section, it was found that the bidirectional DC-DC converters in battery charging applications reduce the voltage stress and current ripples. In particular, several research works previously reported to have implemented the converter's isolated topology. In the isolated topologies, isolation material is required between the conductors and cores for high-frequency transformers. At the same time, insolation is affected by environmental factors and thermal effects [26]. To improve the gain of the converter circuit, the transformer and transfer capacitor is added by the author in [27]. The suggested model has the drawback of the large size of inductors. Hence, the current-fed bidirectional DC-DC converter is proposed in this work to overcome these issues.

The widespread use of EVs has increased the demand for cost-effective and high-speed charging facilities in the EV application. Currently, EV batteries have utilized a significant portion of the EV cost. Hence, more research has been conducted on minimizing switching losses and improving power generation. Although several topologies are developed in this sector, they have some issues, like lower efficiency, switching losses, and high-frequency switching. Moreover, the complexities are increased in the model due to a large number of components and transformer windings. The novelty of this work is the proposed topology of the current-fed DC-DC converter and its controller

To reduce the voltage stress across switches and eliminate voltage spikes at switches, a half-bridge inverter with two main switches is used. Moreover, a full-bridge controlled rectifier with four switches is used in the high-voltage side of the converter. A sliding mode controller was utilized in [28] for reducing uncertainties in DC-to-DC buck converters. Neutral–point–clamped power converters are controlled using sliding mode control with gain adaptation in [29]. Coati-optimized FOPID controllers for non-isolated DC–DC converters in EV charging stations were suggested in [30]. Traditional control techniques, such as proportional–integral (PI) and sliding mode control, have been widely employed to regulate the output voltage and current of converters. However, these techniques often suffer from limitations such as sensitivity to parameter variations, external disturbances, and chattering phenomena. To address these challenges, this paper proposes a novel FOPR controller for DC-DC converters to transfer the power using phase shift modulations for power transfer and pulse width modulation for voltage matching. The proposed FOPR controller offers several advantages over conventional controllers. The operating modes and relevant mathematical equations are modeled for the proposed system. The contribution of the work is given as follows:

- Model current-fed bidirectional DC-DC converter with fewer switches in the EV charging application.
- Enhance the switching pulse generation using the FOPR controller-based pulse width modulation technique.
- Evaluate the converter topology under ZVS and ZCS operating conditions.

The structure of the paper is organized as follows: Section 2 provides some of the related works for bidirectional DC-DC converters with different control strategy. Section 3 explains the proposed methodology with operating modes of the proposed converter and FOPR controller. Section 4 discusses the implemented Matlab results and performance comparison with existing works. Section 5 involves the conclusion and future work.

## 2. Related Works

Some of the existing methods used for EV charging applications with different converters are discussed in this section.

Ranjan and Pati [31] suggested the non-isolated half-bridge topology for the converter used in the EV application. That suggested model was implemented to provide bidirectional flow under normal and abnormal conditions. That model was designed by combining the step-up DC voltage and step-down DC voltage. The control scheme was divided into four blocks to examine the system's condition. The controller blocks 1, 2, 3, and 4 consist of current sensing, error circuit, comparator, and logic gates, respectively. In that model, the converter increases the output voltage to 40 V for 14 V input voltage.

Wu et al. [32] introduced the isolated DC-DC converter with a high gain ratio for EV storage systems. That proposed model was investigated under battery discharging and charging modes under step-up and step-down modes. The proportional–integral–derivative (PID) controller controlled that suggested converter model. The microcontroller unit generated switching pulses to the converter during the variation in input voltage. Thus, that converter model achieved wider and higher voltage gains. Moreover, the switching losses were minimized by the ZVS strategy.

Park et al. [33] proposed the current-fed resonant converter using asymmetric pulse width modulation (APWM). The current-fed models were the boost converter for increasing the power flow. Moreover, it was operated in buck mode for backward power conversion. The APWM strategy regulates the output voltage based on the variations in input voltage. Moreover, the ZVS capability of the model was verified based on the PWM signals and the voltage of the power switch.

Tomar et al. [34] proposed an isolated current-fed bidirectional DC-DC converter in the Reconfigurable Split Battery (RSB) for charging EVs. That converter model can be worked in different charging and discharging modes to charge the RSB voltage source. In discharging mode, voltage gain was high, and the charging of the grid from the batteries was allowed. In charging mode, RSB chooses the corresponding pattern to insert a high current caused by high potential differentiation. Converters were provided with ZVS for MOSFET and ZCS for converter diodes.

Wu et al. [35] proposed the buck–boost current-fed isolated DC-DC converter to reduce the voltage spike and Transient Current Mutation. That suggested model was implemented in the EV chargers and other energy storage systems to provide the buck and boost modes of operation. In addition, the switching algorithm was introduced between the buck and boosted modes of operation to minimize the voltage spikes across the switches. The smooth operation was performed by comparing inductor current control and system control variables.

Piasecki et al. [36] suggested a single active bridge to protect against overvoltage. The simulated model of that suggested converter shows the improvements in that model. A two-level AC-DC converter was initially modeled along with the control strategies on the grid side. The suggested converter model allows galvanic isolation between the EV battery and the main supply. Moreover, the stability was improved by adding multiple parallel modules.

Liu et al. [37] suggested an isolated two-stage energy storage system converter model. That suggested model comprises two converter loops, such as open loop fixed frequency and buck converter for regulating the voltage. An asymmetrical resonant tank was modeled to produce different voltage gains. In the energy storage system application, an integrated transformer with leakage reactance was designed to improve the power density.

The major disadvantage of EVs is the recharging point, which involves short driving range, low speed, battery replacement, and charging duration. Boost chargers with converters and controllers were used to minimize the charge duration [33,38]. The buck–boost converter could not obtain the high voltage gain because of poor efficiency [35]. The flyback converter has drawbacks of more electromagnetic interference, high ripple current, and more losses. Moreover, the bidirectional DC-DC converter has some issues, such as noise, which is more expansive and needs more choppers due to an unstable voltage supply [34]. The existing converter topologies yield voltage stress across the switches, reducing conversion capability. In addition, the buck–boost converters have a lower duty ratio and cannot provide a lower output voltage over a wide input voltage range [28]. Hence, an efficient current-fed converter topology is required for battery charging applications to achieve ZVS and ZCS.

## 3. Proposed Methodology

In this proposed work, a converter is designed for the EV application, which is excited by the voltage source converted to current. This paper aimed to design a current-fed isolated bidirectional DC/DC converter with a novel topology varying the number of switches, capacitors, and transformers from the existing converter topology. The FOPR-controlled modified phase shift pulse width modulation generates the switching signals. A high-frequency transformer isolates the inverter and rectifier of the system. The FOPR-based controller provides switching pulses to the inverter and converter. Switching pulses transfer power from input to output if the output exceeds the reference voltage.

Similarly, if the output voltage exceeds the input side, power is transferred from the output to the input side. The proposed modulation technique smoothens the switching condition of each switch on both the primary and secondary lines of the converter. The novel approach for designing the current-fed bidirectional DC-DC converter is depicted in Figure 1.

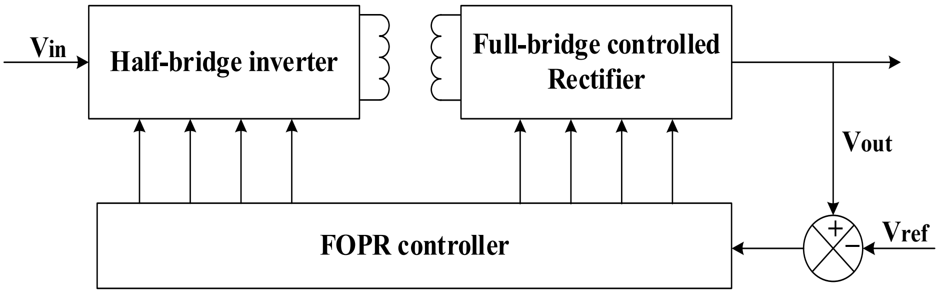

**Figure 1.** Proposed FOPR-controlled current-fed DC-DC converter.

### *3.1. Proposed Current-Fed Isolated Bidirectional DC/DC Converter*

The proposed architecture of the current-fed isolated bidirectional DC-DC converter is depicted in Figure 2. The switching signals for the proposed converter are generated by FOPR-controlled modified pulse width phase shift modulation. $L_1$ and $L_2$ constitute the input inductors, which provide current to the respective switches. The leakage reactance of the transformer $X_{lr}$ is modeled as $L_r$ inductor. The half-bridge inverter consists of the main switches $S_a$ and $S_b$ and the auxiliary switches $S_{a1}$ and $S_{b1}$. A high-frequency step-up transformer is used to isolate the output from the input; further, the purpose of the transformer is to step up the input voltage.

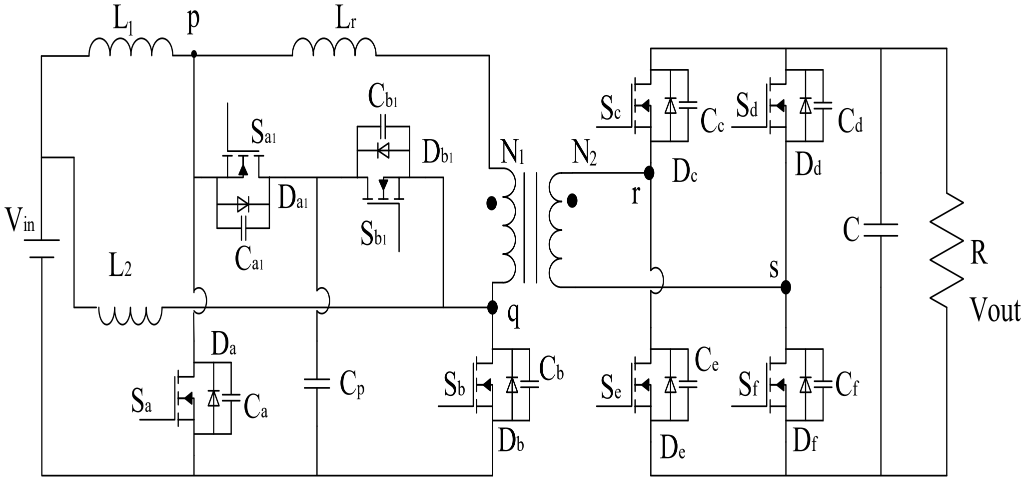

**Figure 2.** Proposed bidirectional DC-DC converter.

The proposed topology of the converter is suitable for vehicular applications, which are excited by a voltage source that is converted into current. The proposed converter topology consists of parallel diodes such as $D_a$, $D_{a1}$, $D_b$, $D_{b1}$, $D_c$, $D_e$, $D_d$, and $D_f$ and parasitic capacitors such as $C_a$, $C_{a1}$, $C_b$, $C_{b1}$, $C_c$, $C_e$, $C_d$, and $C_f$. Moreover, the inductances $L_1$ and $L_2$ are used as current sources, and the leakage inductances $L_r$ are connected to the transformer. The switching cycles are divided into 12 stages. The half switching cycle of the proposed converter is explained in detail. The key waveforms of the proposed converter are depicted in Figure 3.

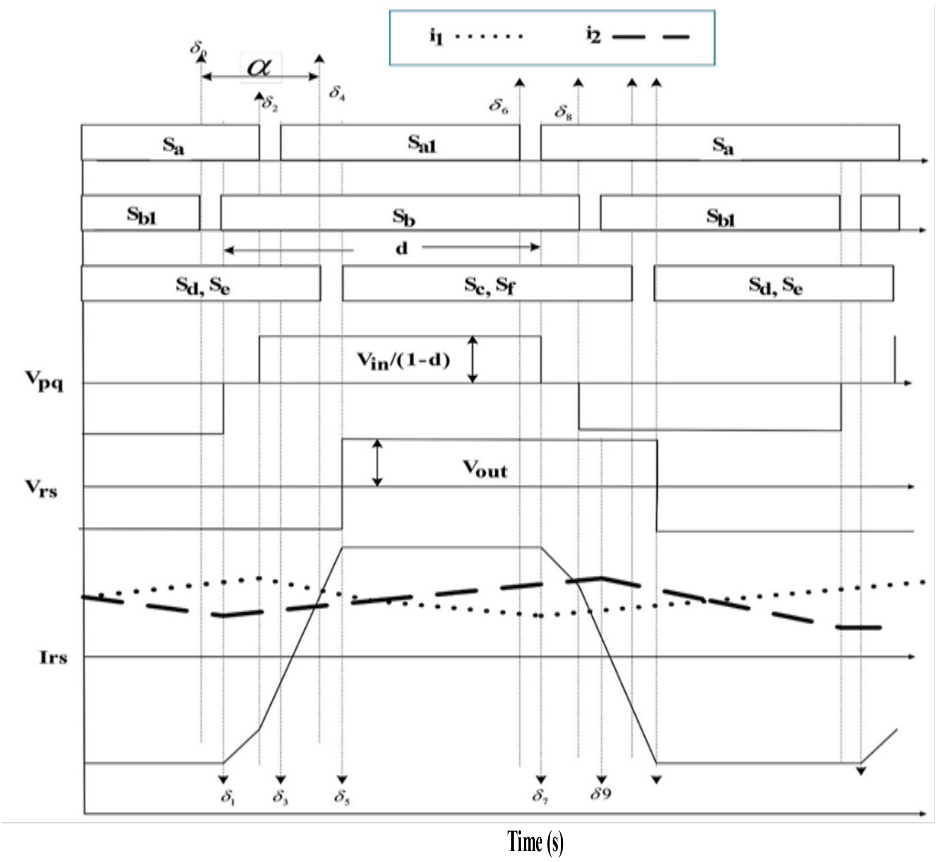

**Figure 3.** Pattern of expected waveforms.

### *3.2. Modes of Operation*

Several modes of operation explain how the proposed converter topology works. The modes of operation of the proposed converter are depicted in Figure 4. Moreover, a detailed explanation of every operating mode is explained below.

- **Mode 0:** In this mode, the switches $S_a$ and $S_{b1}$ are closed on the primary side, and the switches $S_d$ and $S_e$ are closed on the rectifying side or the secondary side converter. The inductor $L_1$ stores energy by the switch $S_a$, and power is transferred from input to output. The current flow through the circuit in mode 0 is depicted in Figure 4a. The equation mentioned below gives the current flowing through the transformer or leakage inductance in this mode.

$$i_{lr} = \frac{-V_{pq}}{X_{lr}} = -I(0) \tag{1}$$

$$X_{lr} = \omega L_r \tag{2}$$

$$\omega = 2 \times \pi \times f \tag{3}$$

where $f$ is the switching frequency, $\omega$ is the angular frequency, $X_{lr}$ is the leakage reactance of the transformer, $L_r$ is the leakage inductance, $i_{lr}$ is the current flow through the transformer, and $V_{pq}$ is the voltage between points $p$ and $q$.

- **Mode 1** ($\delta_0 - \delta_1$)**:** In this mode, at $\delta_0$, the switch $S_{b1}$ is turned off, and switches $S_a$ in the primary side and $S_d$ and $S_e$ in the secondary side are closed. At the instant that $S_{b1}$ is turned off, $L_r$, $C_b$, and $\mathrm{C_{b1}}$ begin to resonate, eliminating the voltage spikes at the switch $S_{b1}$ during turn-off. In the resonance, the condition $C_b$ discharges the energy, and $C_{b1}$ charges. The current flowing through the circuit during mode 1 operation is shown in Figure 4b.
- **Mode 2** ($\delta_1 - \delta_2$)**:** $C_b$ is discharged fully, and therefore, $D_b$ starts conducting. Since $D_b$ is conducting, the voltage across the switch $S_b$ is zero to obtain the ZVS. From the instant of $\delta_1$, the switch $S_b$ can be turned on in the ZVS condition that is mathematically framed in the following equations. In this mode, $S_a$ is conducted on the primary side, and $S_b$ and $S_e$ are closed on the secondary side. $\delta_1 - \delta_2$ is the extra duration in which the main switch conducts for more than 0.5 $d$ ($d$ is the duty cycle). This extra duration is expressed below in terms of the duty cycle.

$$(\delta_2 - \delta_1) = (d - 0.5)2\pi \tag{4}$$

$$\delta_2 = \delta_1 + (d - 0.5)2\pi \tag{5}$$

$$i_{lr}(\delta_{1-2}) = -I(0) + \frac{1}{L_r}\int_{\delta 1}^{\delta} V_{pq} dt \tag{6}$$

$$i_{lr} = -I(0) + \frac{V_{pq}(\delta - \delta_1)}{2X_{lr}} \tag{7}$$

$$V_{pq} = \frac{N_1}{N_2} \times V_{out} \tag{8}$$

$$i_{lr} = -I(0) + \frac{N_1 V_{out}(\delta - \delta_1)}{2N_2 X_{lr}} \tag{9}$$

Here, $\delta$ signifies the time duration, and $N_1$ and $N_2$ are the number of windings in the primary and secondary sides of the transformer. Current in the transformer primary during this mode is expressed in Equation (9). $V_{out}$ is the voltage fed at the load, the same as the transformer's secondary side voltage. The current flowing direction during mode 2 is shown in Figure 4c.

- **Mode 3** ($\delta_2 - \delta_3$)**:** In this mode, at $\delta_2$, the switch $S_a$ is turned off, and the switches $S_b$ in the primary side and $S_d$ and $S_e$ in the secondary side are closed. At the instant $S_a$ is turned off, $L_r$, $C_a$, and $C_{a1}$ begin to resonate, eliminating the voltage spikes at the switch $S_a$ during turn-off. In the resonance, the condition $C_{a1}$ discharges the energy, and $C_a$ will charge. The current flowing through the transformer during this mode is derived as follows.

$$i_{lr}(\delta_{2-3}) = -I(0) + \frac{1}{L_r}\int_{\delta 1}^{\delta 2} V_{pq}dt + \frac{1}{L_r}\int_{\delta 2}^{\delta} V_{pq}dt \tag{10}$$

$$i_{ir}(\delta_{2-3}) = -I(0) + \frac{V_{pq}(d-0.5)2\pi}{2X_{lr}} + \frac{V_{pq}[\delta - \delta_1 - (d-0.5)2\pi)]}{X_{lr}} \tag{11}$$

$$i_{ir}(\delta) = -I(0) + \frac{V_{pq}(d-0.5)\pi}{X_{lr}} + \frac{V_{pq}[\delta - \delta_1 - (d-0.5)2\pi)]}{X_{lr}} \tag{12}$$

$$i_{ir}(\delta) = -I(0) + \frac{N_1 V_{out}(d-0.5)\pi}{N_2 X_{lr}} + \frac{N_1 V_{out}[\delta - \delta_1 - (d-0.5)2\pi)]}{N_2 X_{lr}} \tag{13}$$

The term $(d - 0.5)2\pi$ is the extra duration for which the main switches $S_a$ or $S_b$ are closed during the one-half cycle. The current flowing direction of mode 3 is shown in Figure 4d.

- **Mode 4** ($\delta_3 - \delta_4$)**:** In this mode, $C_{a1}$ is discharged fully, and therefore, $D_{a1}$ starts conducting. Since $D_{a1}$ is closed, the voltage across the switch $S_{a1}$ is zero. From the instant of $\delta_3$, the switch $S_{a1}$ can be turned on in the ZVS condition. The current through the leakage inductance reverses to a positive direction in the middle of this mode. In this mode, $S_b$ is conducted on the primary side, and $S_d$ and $S_e$ are conducted on the secondary side, but both are turned off $\delta_4$. The current flowing direction of mode 4 is shown in Figure 4e.
- **Mode 5** ($\delta_4 - \delta_5$)**:** In this mode of operation, switches $S_e$ and $S_d$ are turned off on the secondary side. On the primary side, $S_b$ and $S_{a1}$ are already in conduction. During this mode, $L_r$, $C_c$, $C_d$, $C_e$, and $C_f$ begin to oscillate. The capacitors of just turned-off switches charge ($C_d$ and $C_e$), and the other two capacitors ($C_V$ and $C_f$) discharge through the leakage inductance of the transformer. The current flowing direction of mode 5 is shown in Figure 4f.
- **Mode 6** ($\delta_5 - \delta_6$)**:** In this mode, diodes $D_c$ and $D_f$ in the secondary side conduct; hence, the voltage across and current through the switches are zero [39–41]. The current flowing direction of mode 6 is shown in Figure 4g.

The equivalent circuit for the resonant condition is shown in Figure 5. The current flowing away from the positive plate of the capacitor $C_b$ means $C_p$ is discharging in a similar way $C_{b1}$ is charging.

Both the current from $i_2$ and $i_{lr}$ is utilized for charging the capacitor $C_b$. The voltage across the capacitor $C_p$ is clamped at $V_{pp}$. This instance is the perfect time to switch on the $S_c$ and $S_f$ switches, which are turned on by both ZVS and ZCS conditions. On the primary side, the $S_b$ and $S_{a1}$ switches are in conduction.

Table 1 shows the details of the mode transition. The above mode explanation is limited only to the first half-cycle, since the circuit is symmetrical. The next half-cycle operation is similar to the first half-cycle.

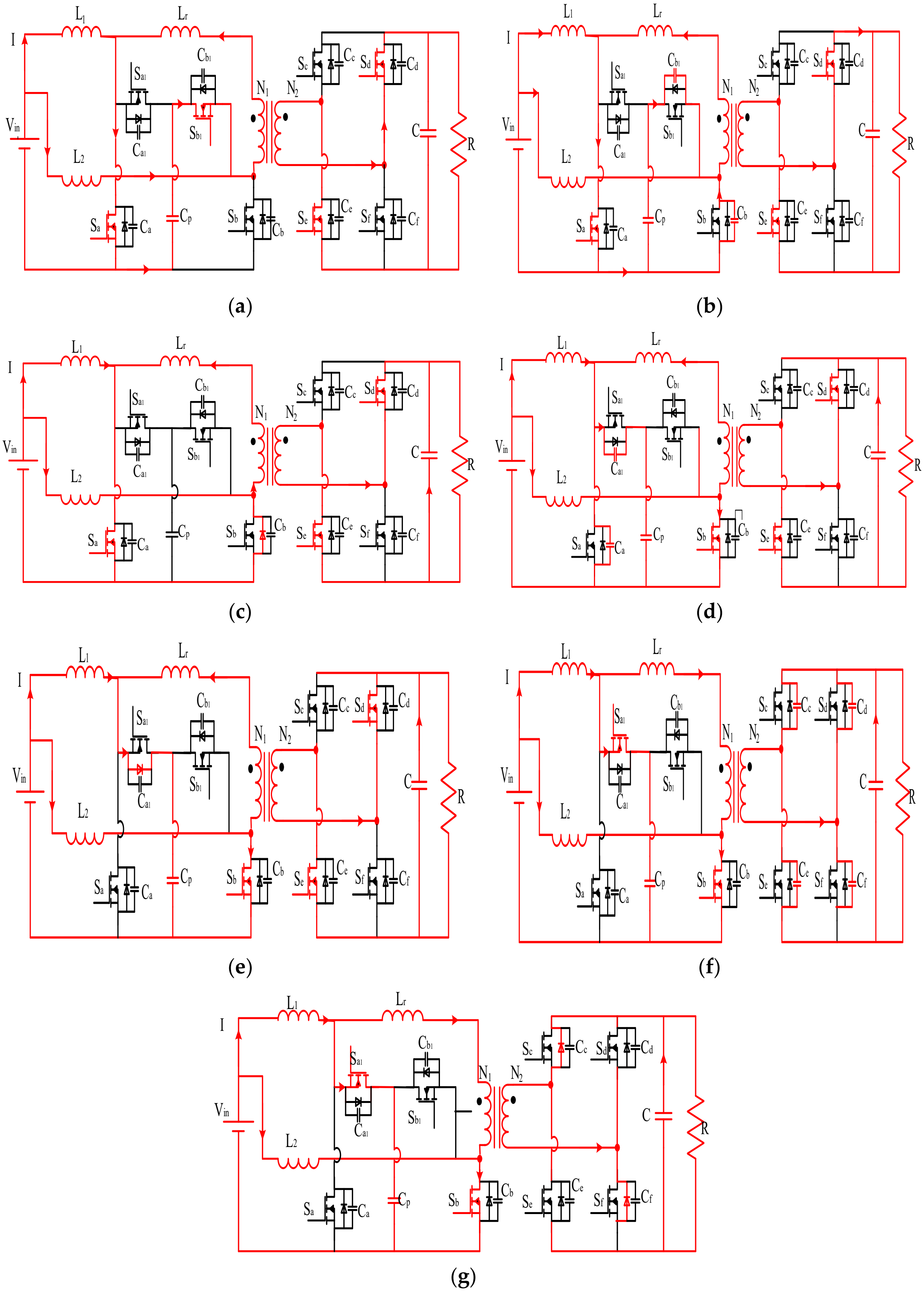

(**a**) (**b**) (**c**) (**d**) (**e**) (**f**) (**g**)

**Figure 4.** Different modes of operation: (**a**) mode 0, (**b**) mode 1, (**c**) mode 2, (**d**) mode 3, (**e**) mode 4, (**f**) mode 5, and (**g**) mode 6.

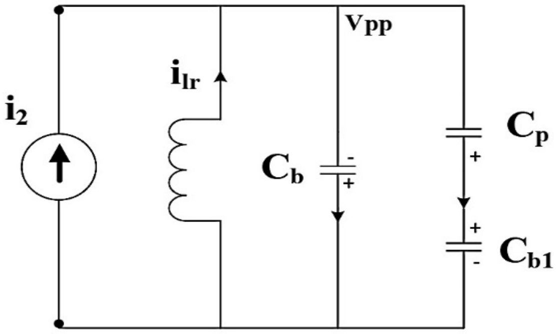

**Figure 5.** Resonant equivalent circuit.

**Table 1.** Details of mode transition.

| Mode Number | Duration (s) | Conduction | Turn ON | Turn OFF |
|---|---|---|---|---|
| Mode 0 | $0 - \delta_0$ | $S_a S_{b1} S_d S_e$ | - | - |
| Mode 1 | $\delta_0 - \delta_1$ | $S_a S_d S_e$ | - | $S_{b1}$ |
| Mode 2 | $\delta_1 - \delta_2$ | $S_a D_b S_d S_e$ | $S_b$ | - |
| Mode 3 | $\delta_2 - \delta_3$ | $S_b S_d S_e$ | - | $S_a$ |
| Mode 4 | $\delta_3 - \delta_4$ | $S_b S_d S_e D_{a1}$ | $S_{a1}$ | - |
| Mode 5 | $\delta_4 - \delta_5$ | $S_{a1} S_b$ | - | $S_d S_e$ |
| Mode 6 | $\delta_5 - \delta_6$ | $S_{a1} S_b D_c D_f$ | $S_c S_f$ | - |

### 3.3. Voltage Matching by Varying Duty Cycle

The following equation gives the transformation ratio of the linear transformer.

$$\frac{N_1}{N_2} = \frac{V_{pq}}{V_{rs}} \tag{14}$$

$V_{rs}$ and $V_{out}$ are the same, substitute these in the above equation as follows:

$$\frac{N_1}{N_2} = \frac{V_{pq}}{V_{out}} \tag{15}$$

The average voltage across the inductors $L_1$ or $L_2$ during the energy storing period ($d$) and energy releasing period $(1 - d)$ is zero, so write it below.

$$V_{in} d + (V_{in} - V_{pq})(1 - d) = 0 \tag{16}$$

Using Equations (15) and (16), the duty cycle for the main switches is calculated as below.

$$d = 1 - \frac{N_2 V_{in}}{N_1 V_{out}} \tag{17}$$

From the above duty cycle equation, for boost mode operation, the duty cycle is more than 0.5. The duty cycle is varied using the pulse width modulation technique to obtain the required output voltage across the load.

### 3.4. Power Transfer by Phase Shift ($\alpha$)

The phase shift angle $\alpha$ is the angle between $V_{pq}$ and $V_{rs}$; by changing the phase shift angle, the magnitude and the direction of power transfer are modulated. If $V_{pq}$ is leading with respect to $V_{rs}$ by an angle of $\alpha$, then power is transformed from input to output. If $V_{rs}$ leads $V_{pq}$ by an angle of $\alpha$, then power is transformed from the output to the input, or the input side battery is charged. As mentioned below, the phase shift range is lag or leads 90 degrees.

$$\alpha \in (-0.5\pi \leq \alpha \leq 0.5\pi) \tag{18}$$

### 3.5. ZVS Condition

The following three conditions control the ZVS of the switches used in the primary side converters for the boost mode of operation.

**Condition 1**

$$|i_{lr}(\delta_0)| > i_2(\delta_0) \tag{19}$$

$$\frac{V_{pq}}{X_{lr}} > \frac{1}{L_2}\int_0^{\beta} V_{in}dt \tag{20}$$

where $\beta$ is $(dT_s)/8$, $T_s$ is the time period of switching frequency, and $d$ is the duty cycle of the main switches.

$$\frac{V_{pq}}{X_{lr}} > \frac{V_{in}}{L_2}\left[\frac{dT_s}{8}\right] \tag{21}$$

From the above equation, it is clear that the magnitude of $I(0)$ should be less than the upper limit of the current flowing through the inductor $L_2$.

**Condition 2**

When the main switch $S_a$ is switched off, the current through the transformer should be less than the current through the inductor $L_2$.

$$i_{lr}(\delta_2) < i_2(\delta_2) \tag{22}$$

$$-I(0) + \frac{N_1 V_{out}(d-0.5)\pi}{N_2 X_{lr}} < \frac{V_{in}}{L_2}\left[\frac{dT_s}{8}\right] \tag{23}$$

**Condition 3**

In this instant, the transformer current should reverse its direction completely.

$$i_{lr}(\delta_4) > 0 \tag{24}$$

The main switch $S_b$ should be switched on to satisfy this condition by controlling the angle $\alpha$.

### 3.6. Control Strategy Using FOPR Controller

The magnitude and direction of the transferred power are controlled by varying the phase shift angle $\alpha$, whereas voltage matching is conducted by varying the pulse width modulation of the duty cycle $d$ of the two main switches $S_a$ and $S_b$.

$$V_{out} = \frac{N_2 V_{in}}{N_1(1-d)} \tag{25}$$

$$P_{out} = \frac{N_1 V_{in} V_{out} \alpha(\pi-\alpha)}{N_2 X_{lr}\pi}\,W \tag{26}$$

The power transfer from the low voltage input side to the load side is performed by boost mode, whereas reverse power transfer is performed by buck mode of conduction. The FOPR-based controller is implemented to perform the voltage and power modulations [42]. The basic block of the FOPR controller is given in Figure 6.

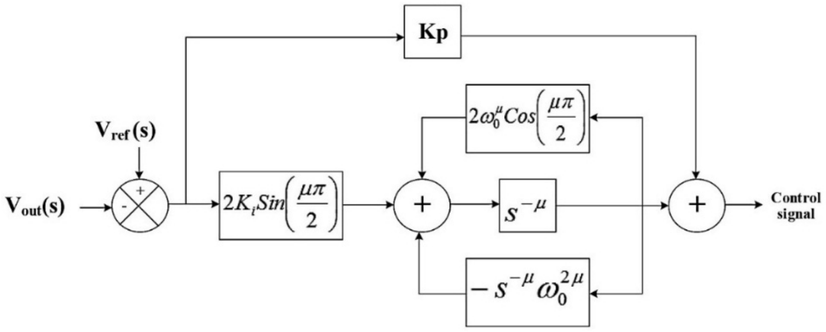

**Figure 6.** FOPR controller.

In the proposed system, a DC voltage source is applied as input; generally, a bidirectional DC-DC converter battery is fed as input. Bidirectional converters are used in those practical applications, since the battery delivers and charges the power sequentially. The converter operates in boost mode when the output voltage exceeds the reference set voltage. The transformer's primary and secondary side voltage is matched by varying the pulse width variation of the duty cycle. Power is transferred from the input low-voltage side to the output high-voltage side.

The output of the FOPR controller is the outcome of adding three terms, of which two depend on the controller's output and one term depends on the error signal. The diagrammatic representation of the FOPR controller implemented in this present work is shown in the figure above. Here, $K_p$ and $K_i$ are constants, $\omega_0$ is the angular switching frequency, and $\mu$ is a fractional number. The FOPR controller's advantages are wider bandwidth and maximum gain for the selected frequency.

### *3.7. Design Calculation*

- ➢ Output voltage

The voltage at the higher end of the proposed converter is obtained by applying the values of Equation (25).

$$V_{in} = 25 \tag{27}$$

$$\frac{N_2}{N_1} = 2 \tag{28}$$

$$d = 0.55 \tag{29}$$

$$V_{out} = 111.11V \tag{30}$$

The output voltage is calculated for a duty ratio of 55 percent of the main switches with a transformation ratio of 2. The input voltage range is used here from 18 V to 25 V upper limit. Hence, the battery is in discharging mode.

- ➢ Leakage reactance of the transformer

The leakage reactance of the step-up transformer is an important part of the proposed system. Its value is obtained from the output power equation mentioned in Equation (26). The output power of 2 KW is designed, and a phase shift angle of $\alpha$ = 30 is considered for designing the leakage reactance of the step-up transformer.

$$2000 = \frac{25 \times 111 \times 0.523(3.14 - 0.523)}{2 \times X_{lr} \times 3.14} \tag{31}$$

$$X_{lr} = 0.3023\,\Omega \tag{32}$$

A higher frequency of 100 kHz is employed in the inverter stage, which is provided to design the transformer leakage reactance.

$$2 \times \pi \times f \times L_r = 0.3023\,\Omega \tag{33}$$

$$L_r = 49\mu H \tag{34}$$

- ➢ Calculation of maximum transformer current

The maximum current that flows through the transformer's leakage reactance is obtained from Equation (1).

$$V_{pq} = \frac{V_{in}}{1-d} \tag{35}$$

Here, $V_{pq}$ is the voltage across the primary side of the transformer, which is calculated from the duty cycle of the main switches.

$$V_{pq} = \frac{25}{(1-0.55)} \tag{36}$$

$$V_{pq} = 56V \tag{37}$$

$$i_{lr} = \frac{56}{0.3023} \tag{38}$$

Here, $i_{lr}$ = 184 A; this is the maximum limit of inductor current passing through the leakage reactance of the transformer.

- ➢ Input inductors

The input inductors $L_1$ and $L_2$ are designed based on the switching frequency duty cycle and its permissible ripple voltage.

$$L_x = \frac{V_{in}d}{\Delta i_x F_s F} \tag{39}$$

$$L_x = \frac{25 \times 0.55}{18 \times 100 \times 10^3} H \tag{40}$$

$$L_x = 8.5\mu H \tag{41}$$

The input inductor values are calculated for a duty cycle of 55 percent with 18 A ripple.

## 4. Simulation Results

The proposed bidirectional current-fed DC-to-DC converter model's simulation model is shown below. The simulation for the proposed converter is performed by using Matlab/Simulink. The Simulink block of the proposed work is shown in Figure 7.

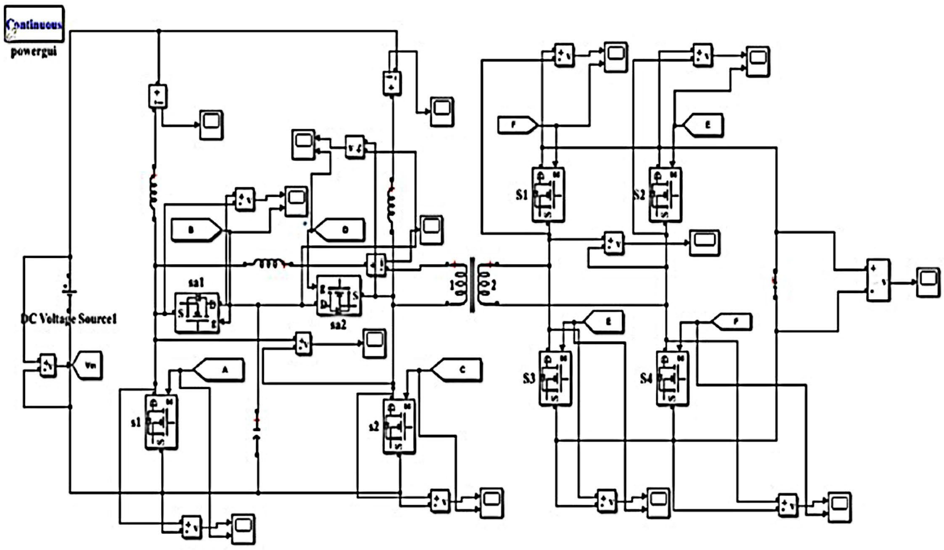

**Figure 7.** Simulation model for the proposed DC-to-DC converter.

FOPR is used to provide a switching sequence based on the mode of charging or discharging. The converter operates in boost mode during the discharging mode, and the converter operates in buck mode for charging. The parameters used in the simulation are mentioned in Table 2.

**Table 2.** Simulation parameters.

| Parameter | Symbol | Value |
|---|---|---|
| Input voltage | $V_{in}$ | 25 V |
| Output voltage | $V_{out}$ | 111 V |
| Switching frequency | $F_5$ | 100 kHz |
| Transformation ratio | N1: N2 | 1:2 |
| Input inductance | $L_1$ | 8.5 µH |
| Input inductance | $L_2$ | 8.5 µH |
| Leakage reactance | $L_r$ | 90 µH |
| Clamping capacitor | $C_p$ | 2.6 µF |
| Output capacitor | $C$ | 10 µF |
| Duty cycle | $d$ | 0.55 |
| Proportional constant | $K_p$ | 0.5 |
| Integral constant | $K_i$ | 0.6 |
| Fractional order | $\mu$ | 0.6 |
| Selected angular frequency | $\omega_0$ | $6.18 \times 10^5$ rad/s |

### 4.1. Discharging Boost Mode

The voltage across the primary and secondary side transformer is shown in Figure 8. The output voltage across the respective transformer matches well with the expected pattern of the output waveform. The results show that the voltage across the secondary side is increased more than the primary side of the transformer when the converter is in boost mode.

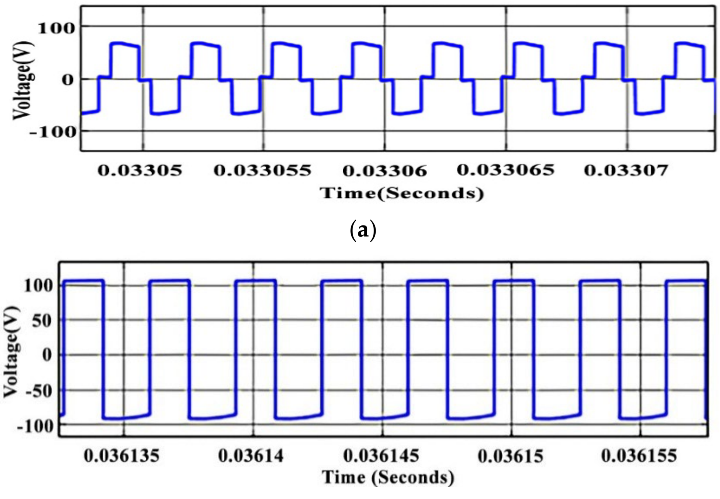

(**a**)

(**b**)

**Figure 8.** Transformer voltage. (**a**) Primary side and (**b**) secondary side.

In the proposed converter, a high switching frequency boosts the output voltage with a reduced input inductance value. Hence, the weight of the inductor and the transformer core area subsequently decreased the cost. The current measured at the inductor is shown in Figure 9.

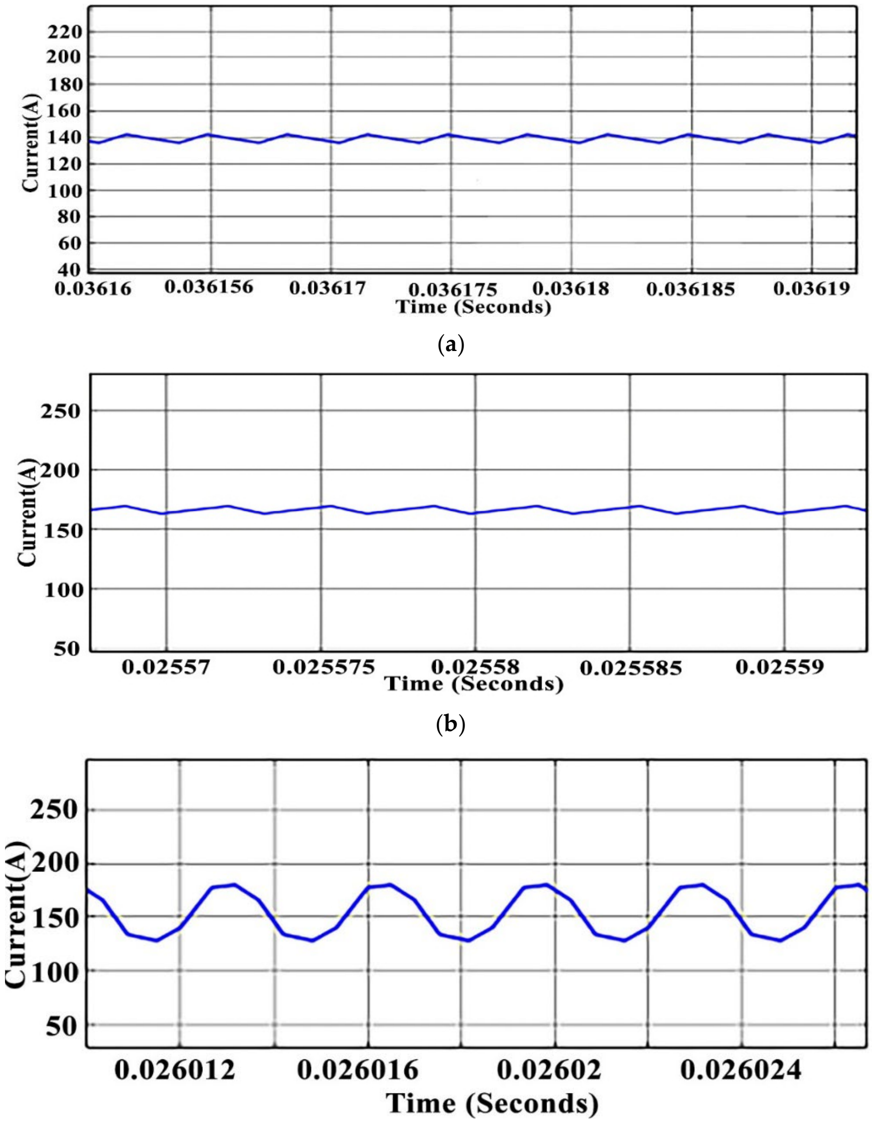

(**a**)

(**b**)

(**c**)

**Figure 9.** Current through the inductor. (**a**) $L_1$, (**b**) $L_2$, and (**c**) leakage reactance.

The pattern of the waveforms matches well with the expected current waveforms. From the diagrams, the instant of $\delta_0$, the inductor current $L_2$ is lesser than the magnitude of the current flowing through the leakage reactance. Also, $\delta_2$, the current through the leakage inductor is less than the input inductor $L_2$ during the instant. Hence, the conditions for ZVS are satisfied, and all the switches will operate in ZVS conditions. The small amount of current circulation allows the diode to conduct to ensure ZCS operation.

In most cases, ZCS is achieved while ZVS is a turn-off. Similarly, the conditions are applied for ZCS, and the switches are operated in ZCS conditions. Since the conditions are satisfied, all the switches, both on the inverting side and rectifying side switches, are operated in ZVS further by utilizing the output capacitance for the resonant circuit, and the voltage spikes at the switches are eliminated. The voltage spikes are reduced and turned on at ZVS using the FOPR controller. The voltage stress at the main switch $S_a$ and $S_b$ during on time is only 50 V. Figures 10–13 depict the voltage stress at switches $S_a$, $S_{a1}$, $S_b$, $S_{b1}$, $S_c$, $S_f$, $S_d$, and $S_e$. Since the inductors are selected based on the condition for ZVS and ZCS, spikes across the switches are eliminated by utilizing the output capacitance for resonant circuit voltage.

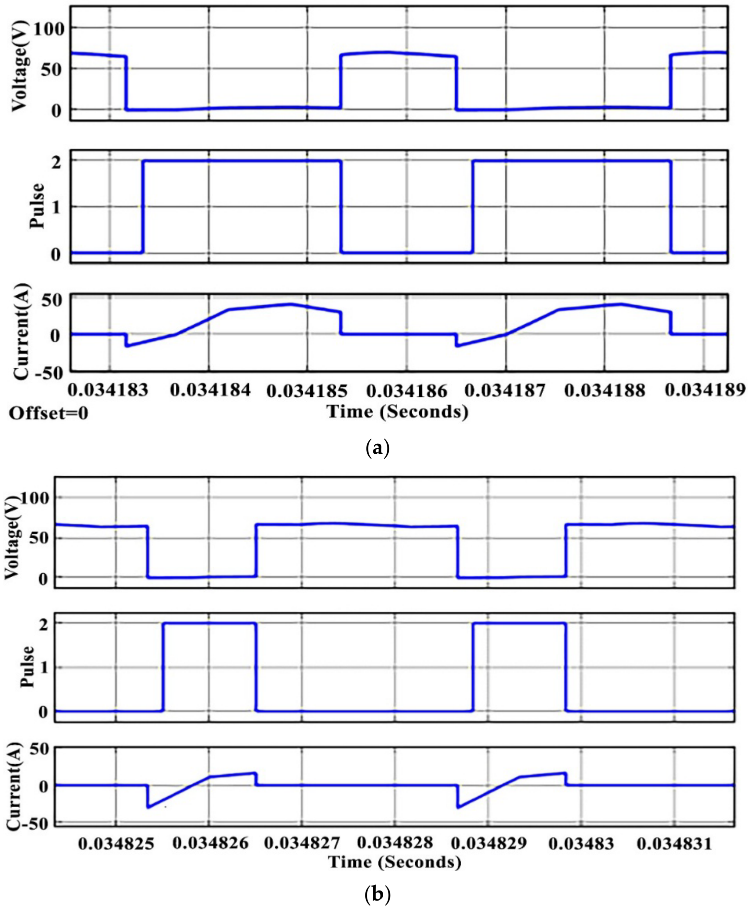

(**a**)

(**b**)

**Figure 10.** Gate pulse, voltage, and current through switches $S_a$ and $S_{a1}$ during (**a**) turn-on and (**b**) turn-off.

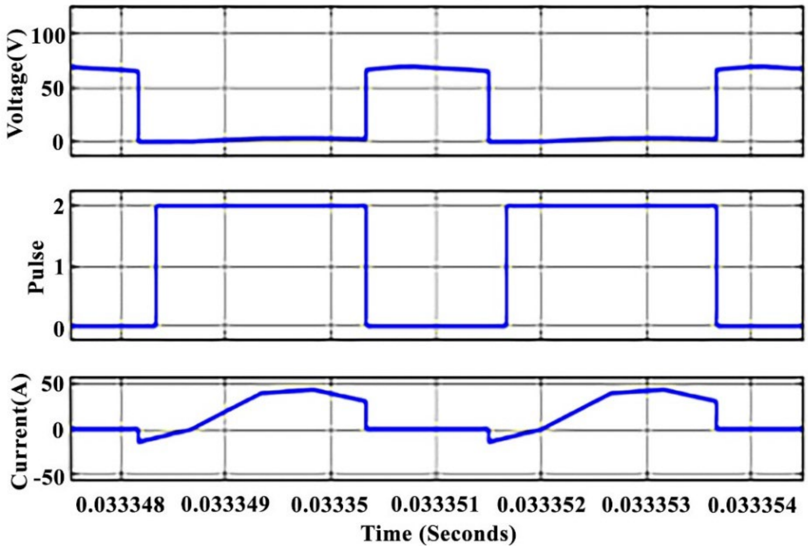

(**a**)

**Figure 11.** *Cont.*

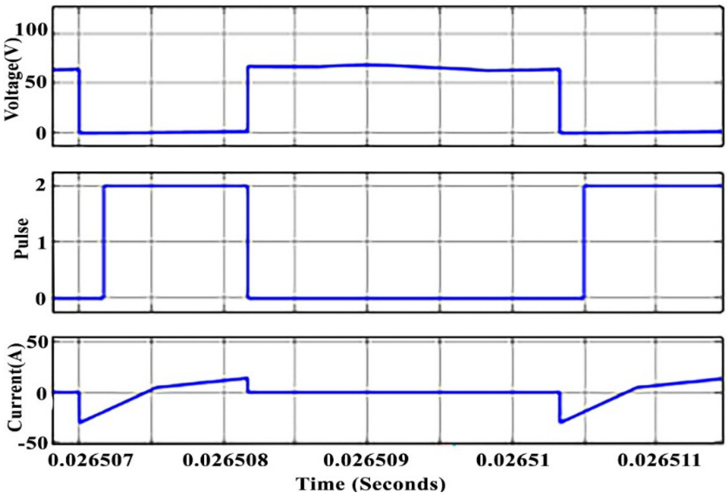

(**b**)

**Figure 11.** Gate pulse, voltage, and current through switches $S_b$ and $S_{b1}$ during (**a**) turn-on and (**b**) turn-off.

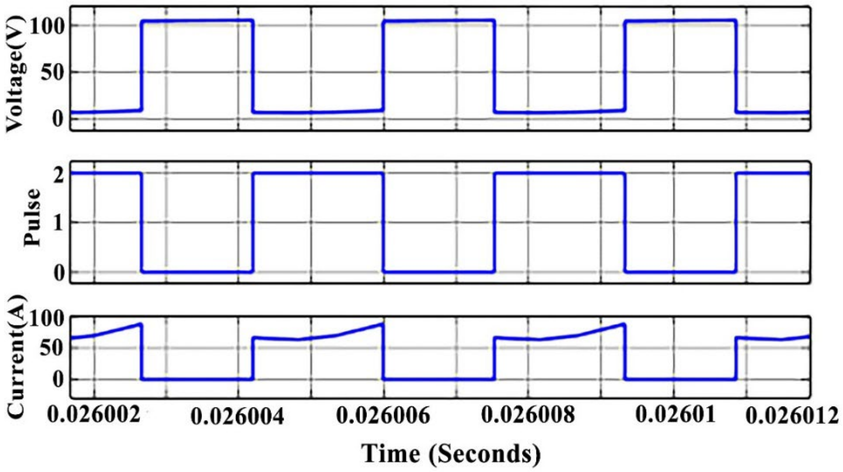

(**a**)

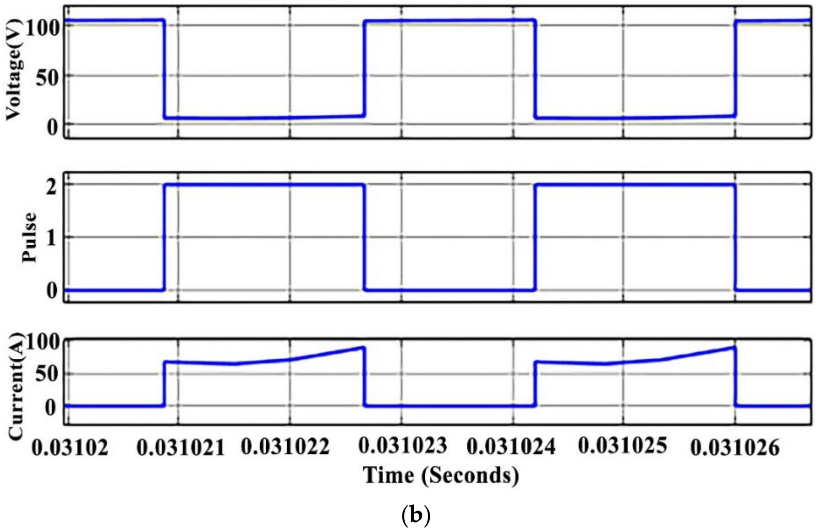

(**b**)

**Figure 12.** Gate pulse, voltage, and current through switches $S_c$ and $S_e$ during (**a**) turn-on and (**b**) turn-off.

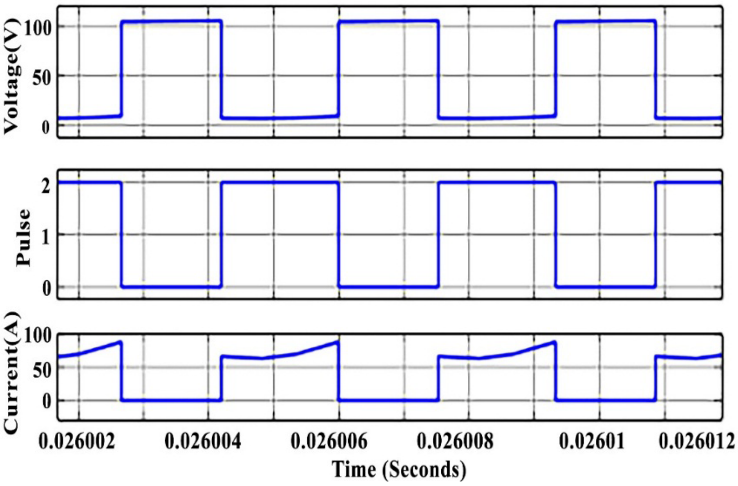

(**a**)

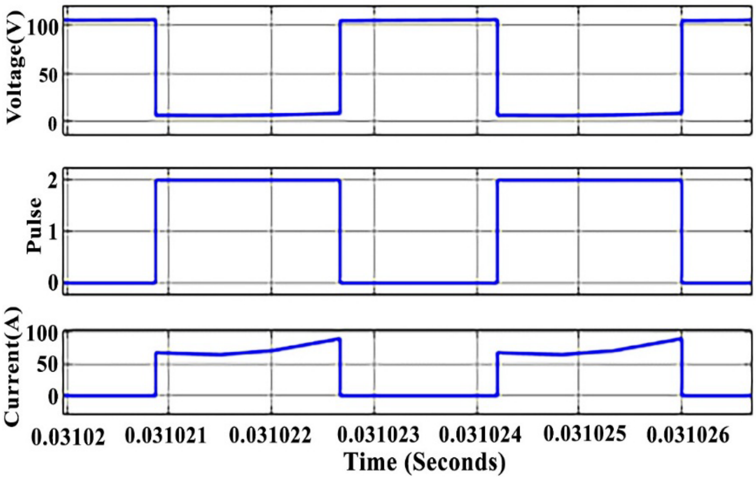

(**b**)

**Figure 13.** Gate pulse, voltage, and current through switches $S_d$ and $S_e$ during (**a**) turn-on and (**b**) turn-off.

The output rectified voltage is shown in Figure 14. Using the FOPR controller, the power is transformed from input to output in the boost mode of operation. Using the FOPR-based modulation technique, the output voltage and the transferred power are controlled elegantly.

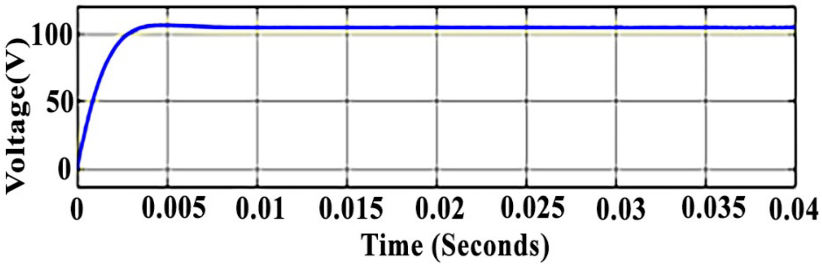

**Figure 14.** Output voltage in discharging of battery (boost mode).

From the results, it is verified that the proposed FOPR has improved the switching pulse generation for all the switches in the converter topology, thereby minimizing the stress on switches.

### *4.2. Recharging Buck Mode*

The power transfer is reversed in the recharging buck mode by reversing the phase shift angle $\alpha$. In this mode, the DC voltage of 240 V is converted to the high-frequency alternating voltage across primary and secondary windings in the transformer. The voltage across the primary is measured at around 73 V, as shown in Figure 15.

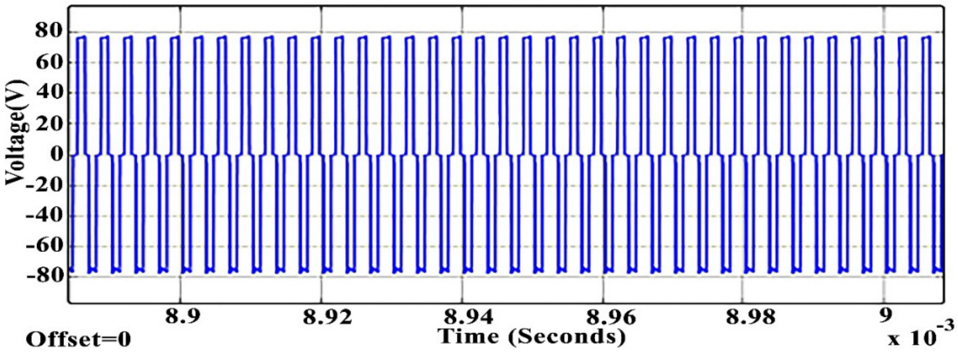

**Figure 15.** Voltage across primary transformer in recharging mode.

The power is transferred from the secondary side's high voltage to the primary side's low voltage. The converter between the secondary and primary sides can act as a boost converter in discharging mode and a buck converter in charging mode. The negative direction of the current implies the power in the reverse direction. The average charging current of the battery is around 5 A, which flows through the input low-voltage side. Figure 16 shows the flow of current in the buck mode.

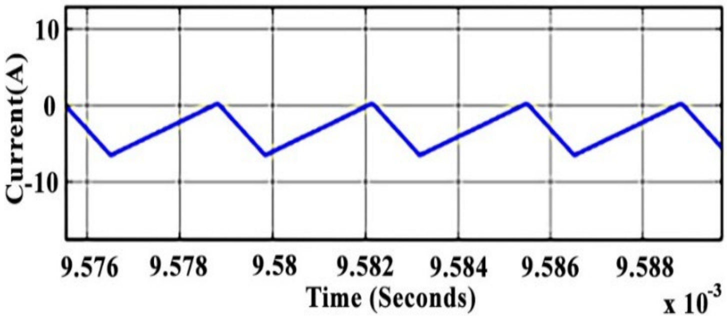

(**a**)

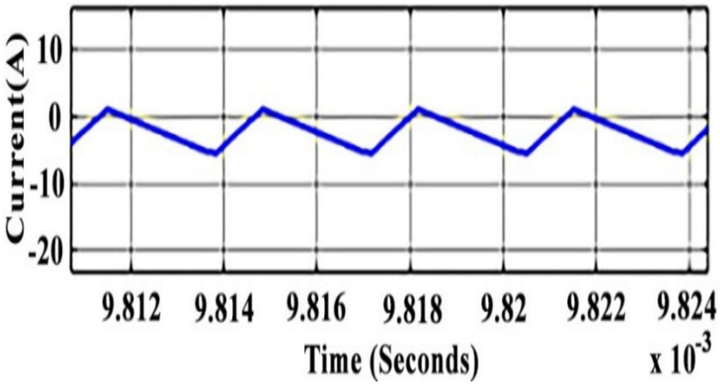

(**b**)

**Figure 16.** *Cont.*

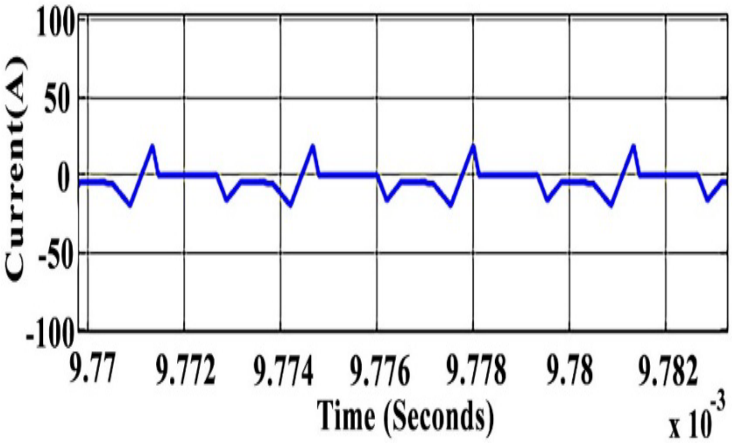

(**c**)

**Figure 16.** Current flows through the inductor in recharging mode. (**a**) $L_1$, (**b**) $L_2$, and (**c**) leakage reactance.

Figures 17–20 depicts the voltage stress at switches $S_a$, $S_{a1}$, $S_b$, $S_{b1}$, $S_c$, $S_d$, $S_e$, and $S_f$ during the buck mode of operation. Since the inductors are selected based on the condition for ZVS and ZCS, the output capacitance for resonant circuit voltage spikes across the switches is eliminated.

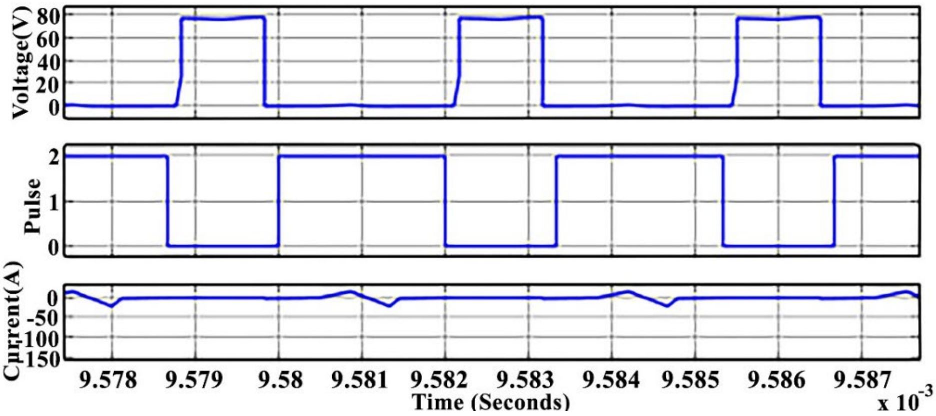

(**a**)

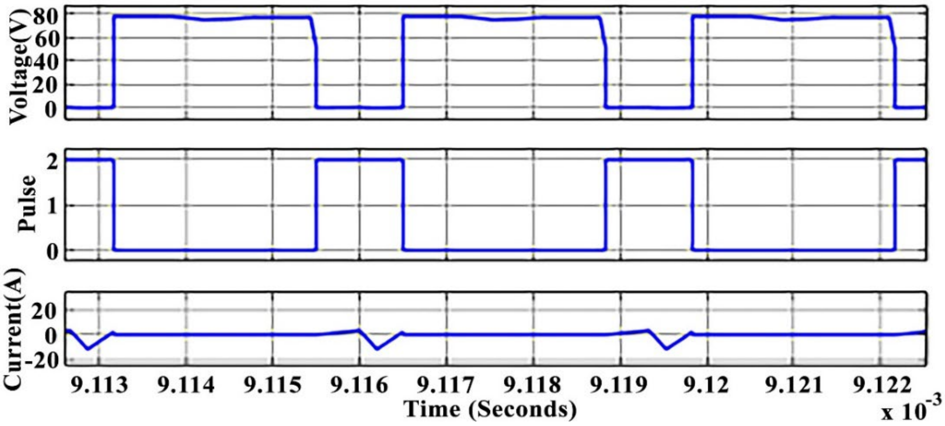

(**b**)

**Figure 17.** Gate pulse, voltage, and current through switches $S_a$ and $S_{a1}$ during (**a**) turn-on and (**b**) turn-off in recharging mode.

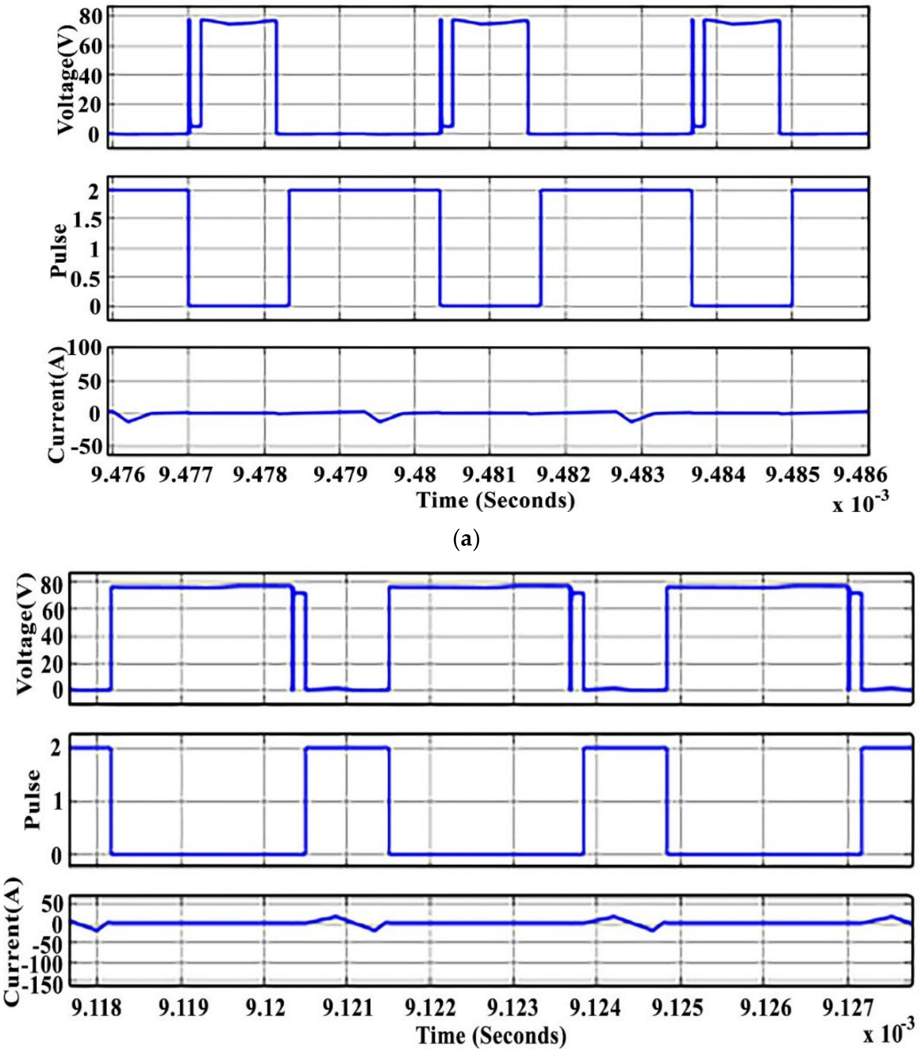

(**a**)

(**b**)

**Figure 18.** Gate pulse, voltage, and current through switches $S_b$ and $S_{b1}$ during (**a**) turn-on and (**b**) turn-off in recharging mode.

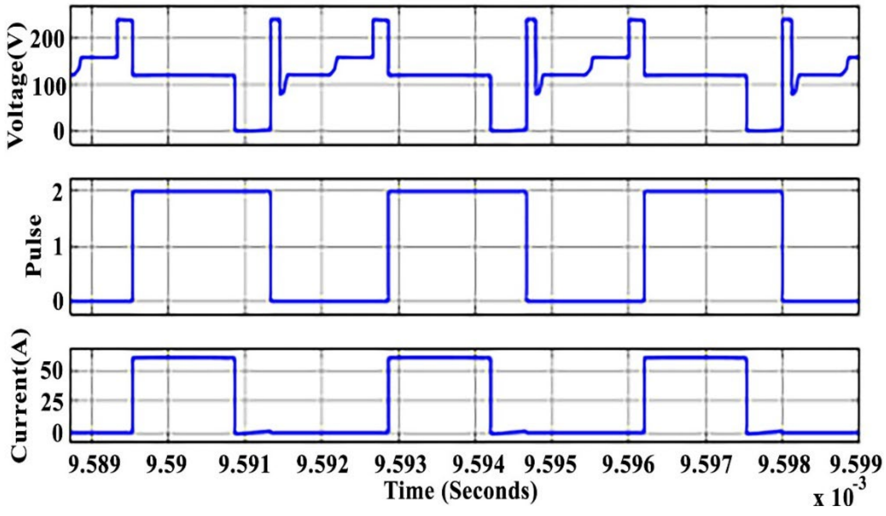

(**a**)

**Figure 19.** *Cont.*

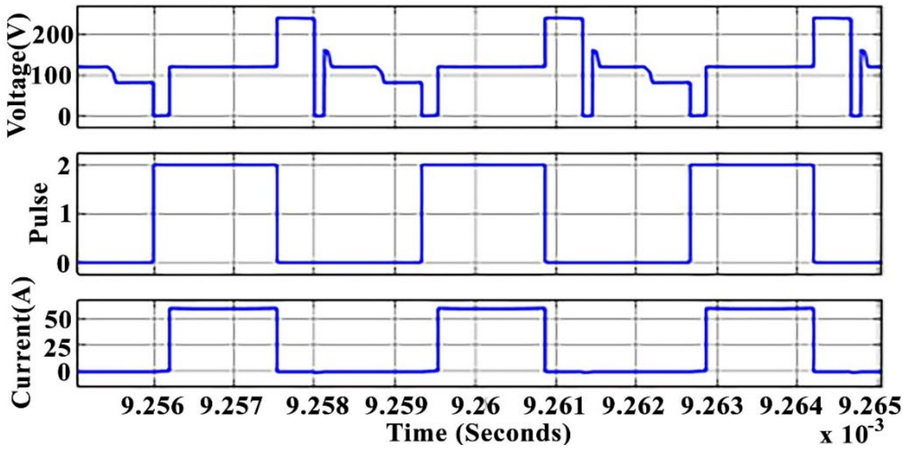

(**b**)

**Figure 19.** Gate pulse, voltage, and current through switches $S_c$ and $S_f$ during (**a**) turn-on and (**b**) turn-off in recharging mode.

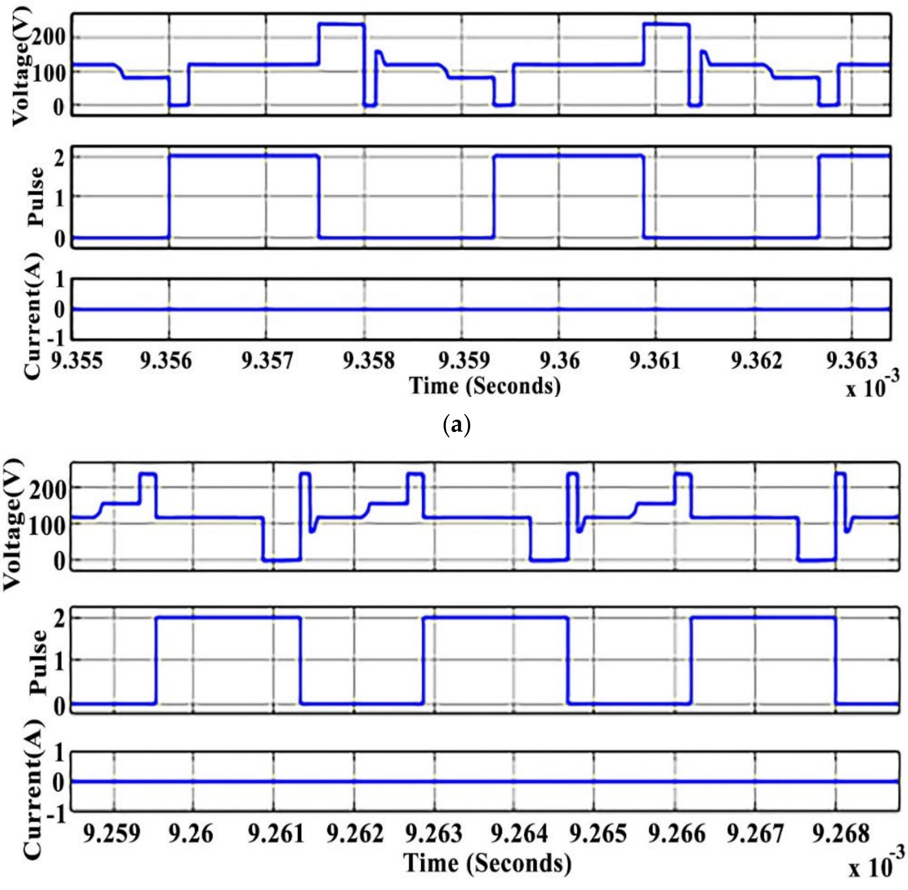

(**a**)

(**b**)

**Figure 20.** Gate pulse, voltage, and current through switches $S_d$ and $S_e$ during (**a**) turn-on and (**b**) turn-off in recharging mode.

The rectified output voltage in the recharging mode of the battery is shown in Figure 21. It shows that the recharging mode of the battery will provide a voltage rating of 24 V. Using the FOPR-based control strategy, the current and voltage are controlled in the network.

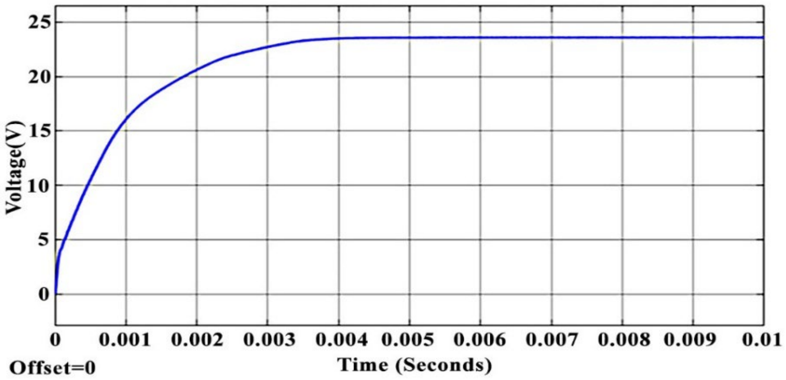

**Figure 21.** Output voltage in recharging of battery (buck mode).

The voltage spike on converter switches will reduce the conversion efficiency of the converter [43], as the voltage spikes occur due to imbalance voltages or light load conditions. The modulation techniques will avoid spikes over high-power and high-voltage applications. The voltage spike reduction by the proposed methodology is shown in Figure 22, as it shows that the proposed FOPR-based modulation technique reduces the voltage spikes in the converter without switching losses.

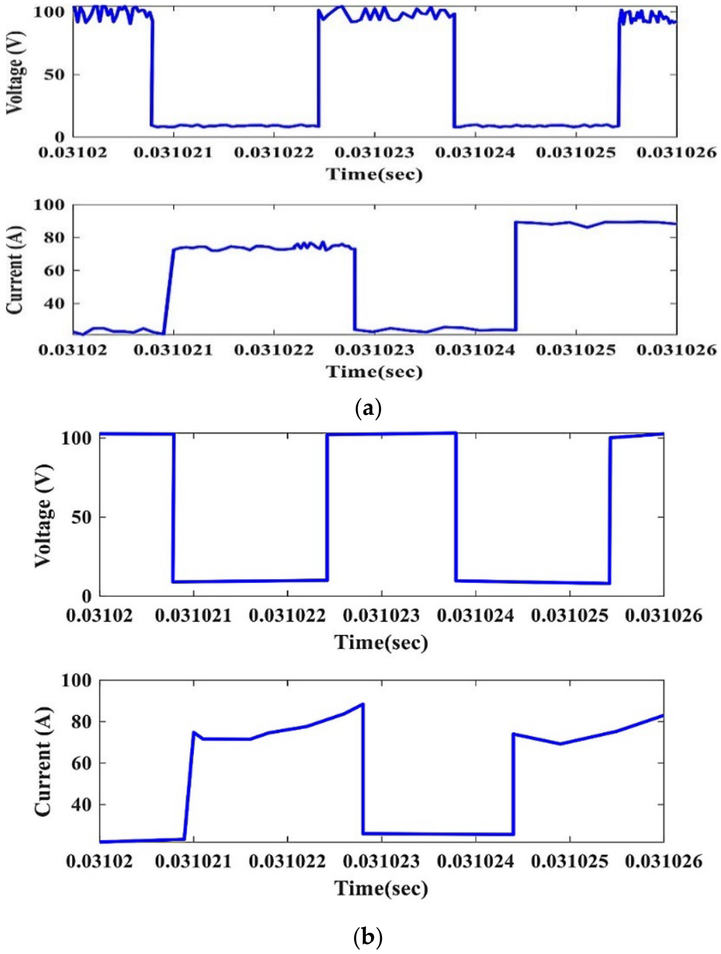

**Figure 22.** Voltage waveform (**a**) during spikes and (**b**) with proposed FOPR.

### 4.3. Discussion

In this section, the proposed work is compared with existing converter topologies in a bidirectional isolated converter [32], current-fed bidirectional converter [34], two-stage converter [37], novel isolated converter [43], high step-up/-down converter [44], and ZVS bidirectional converter [45]. The comparative analysis of voltage gain in Figure 23 indicates that the proposed controller had a higher voltage gain; thus, it can be used in numerous high-power applications. Therefore, the suggested converter topology and modulation technique are well suited for EV charging applications.

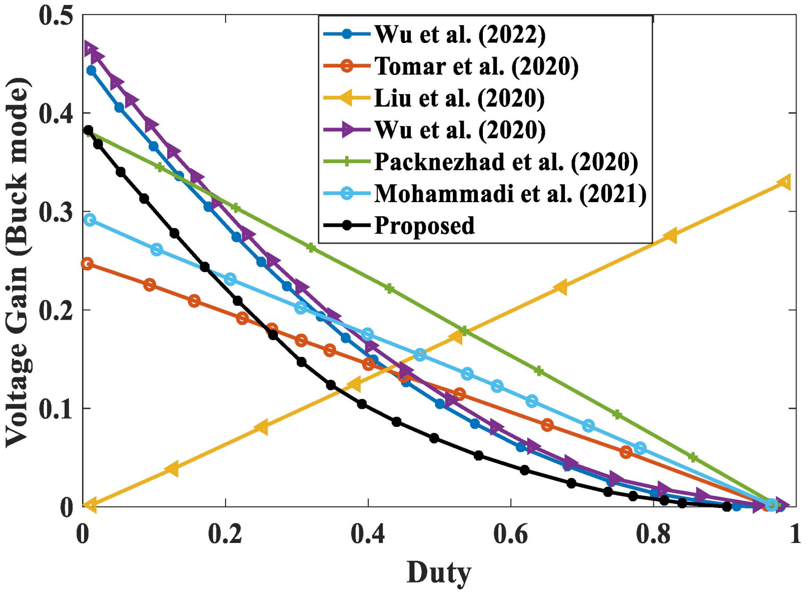

(**a**)

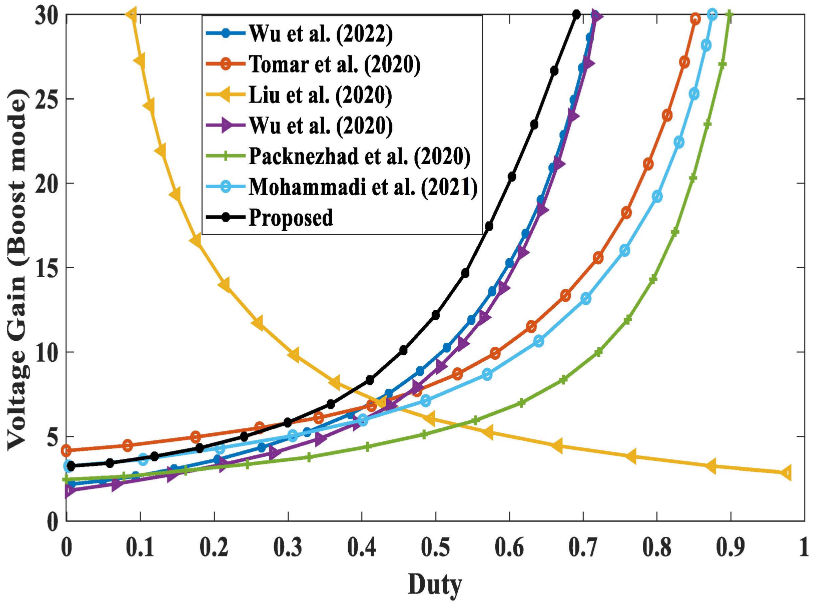

(**b**)

**Figure 23.** Comparative analysis of voltage gains [32,34,37,43–45]. (**a**) Buck mode and (**b**) boost mode.

The comparative analysis of converter efficiency is shown in Figure 24. The converter topology used in [34] does not have enough conversion efficiency to provide only lower power at the output. Whereas the converter topology used in [37] has better efficiency, it has many components. Compared to these converter topologies, it is verified that the proposed topology has higher efficiency than other topologies.

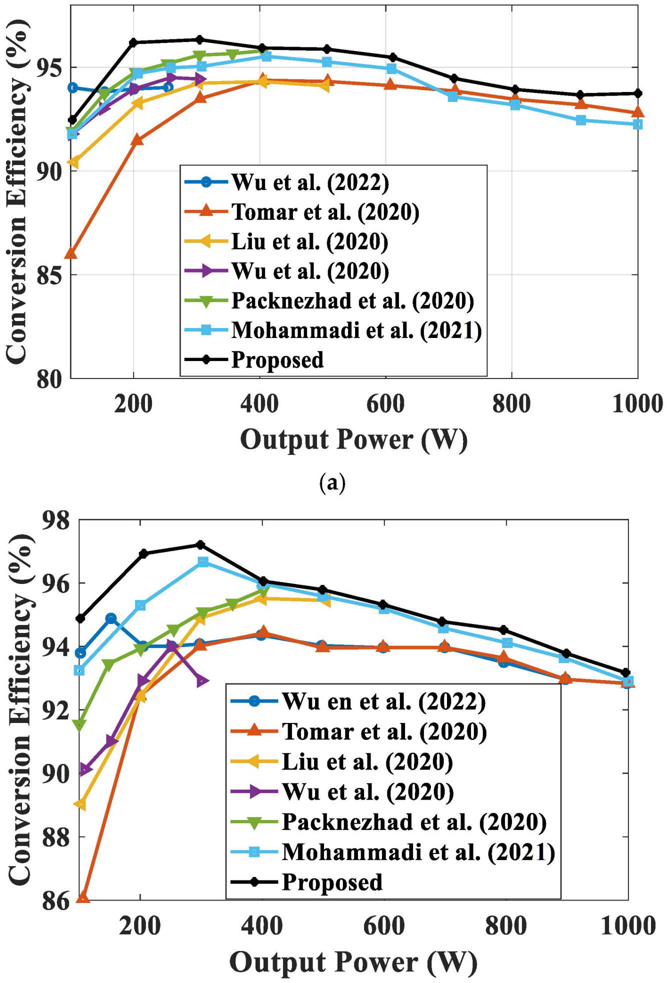

(**a**)

(**b**)

**Figure 24.** Comparative analysis of conversion efficiency [32,34,37,43–45]. (**a**) Buck mode and (**b**) boost mode.

Table 3 presents a comparison of power loss in various components of a power electronic converter for existing methods. By analyzing the power loss values, we can assess the relative performance and efficiency of these designs. The proposed design demonstrates lower power losses in all components compared to the reference designs, suggesting improved efficiency and potentially lower operating costs. Lower power losses in individual components can lead to improved overall system efficiency, reduced component stress, smaller and lighter systems, and lower operating costs.

**Table 3.** Comparative analysis of losses.

| Types of Loss | [32] | [43] | [44] | Proposed |
|---|---|---|---|---|
| MOSFET loss | 88.74 W | 8.13 W | 66 W | 8 W |
| Magnetic component loss | 10.6 W | 31.16 W | 11 W | 10.35 W |
| Capacitor loss | 11.3 W | 39.81 W | 4 W | 8 W |
| Line loss | 7.35 W | 20.90 W | 8 W | 7.98 W |

The comparative analysis of voltage spike reduction using the optimized duty cycle modulation strategy [46] and hybrid modulation [47] is shown in Figure 25. The comparative analysis shows that the existing methods have not reduced the spikes at a considerable level. The proposed method significantly minimizes the voltage spikes to the minimum level.

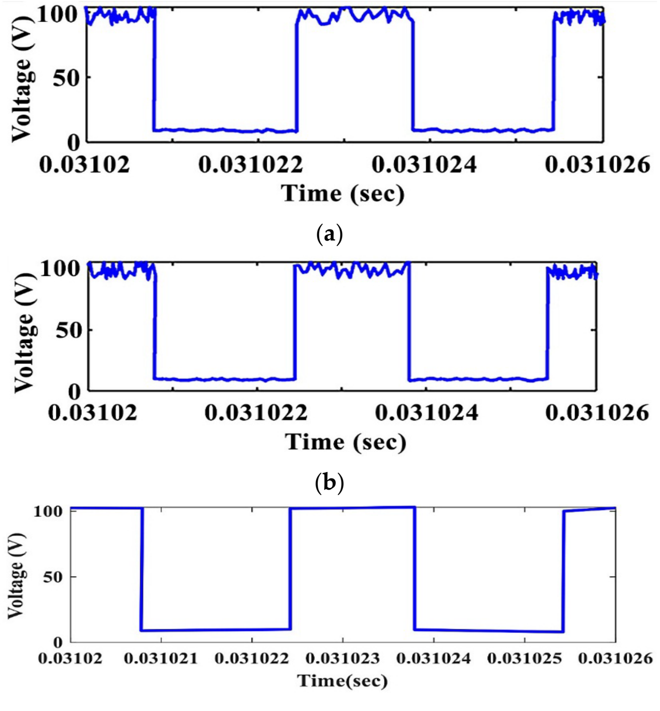

(**a**)

(**b**)

(**c**)

**Figure 25.** Comparative analysis of voltage spike reduction. (**a**) Optimized duty cycle modulation strategy [46], (**b**) hybrid modulation [47], and (**c**) proposed method.

## 5. Conclusions

This paper proposes a novel bidirectional current-fed DC-DC converter for the EV charging application. Here, the converter is designed with eight switches, and the proposed FOPR-based pulse width modulation strategy provides the controlling pulses. Moreover, the ZVS and ZCS conditions are verified in the converter model during no-load and full-load conditions. The ZVS is achieved by adding a clamping capacitor with the auxiliary switches. The proposed work is implemented on the Matlab/Simulink model, and the results are verified in terms of charging and discharging modes. The inductor current and output voltage are verified for both the charging and discharging modes of operations. In this proposed topology, the voltage spikes are minimized by the output capacitance and high-frequency transformer leakage. Moreover, the turn-on voltage of the converter is lower in both the buck and boost modes of operation. Due to the lower turn-on voltage, the voltage spikes in the system are reduced. Moreover, the results imply that the proposed topology is more effective for high-efficiency power converter applications through reduced switching losses. While experimental validation is crucial, the comprehensive simulation analysis provides strong evidence of the converter's potential. Future work will focus on hardware prototyping, advanced control strategies, and multi-mode operation to further enhance the converter's capabilities and real-world applicability.

**Author Contributions:** Conceptualization, P.S. and D.K.P.; methodology, A.K.S. and Y.G.; software, P.S.; validation, D.K.P., Y.G. and J.C.R.-C.; formal analysis, Y.G. and J.C.R.-C.; investigation, J.C.R.-C.; resources, Y.G. and J.C.R.-C.; data curation, Y.G. and J.C.R.-C.; writing—original draft preparation, P.S.; writing—review and editing, P.S., D.K.P., A.K.S., Y.G. and J.C.R.-C.; visualization, Y.G. and J.C.R.-C.; supervision, J.C.R.-C.; project administration. All authors have read and agreed to the published version of the manuscript.

**Funding:** This research received no external funding.

**Data Availability Statement:** Data sharing not applicable to this article.

**Conflicts of Interest:** The authors declare no conflict of interest.

## References

1. Zhang, G.; Li, Z.; Zhang, B.; Halang, W.A. Power electronics converters: Past, present and future. *Renew. Sustain. Energy Rev.* **2018**, *81*, 2028–2044. [CrossRef]
2. Sharma, P.; Dhaked, D.K.; Sharma, A.K. Mathematical modeling and simulation of DC-DC converters using state-space approach. In Proceedings of the Second International Conference on Smart Energy and Communication: ICSEC 2020, Jaipur, India, 20–21 March 2020; Springer: Singapore, 2021; pp. 11–29.
3. Lu, Y.; Wu, H.; Sun, K.; Xing, Y. A family of isolated buck-boost converters based on semiactive rectifiers for high-output voltage applications. *IEEE Trans. Power Electron.* **2015**, *31*, 6327–6340. [CrossRef]
4. Sharma, P.; Sharma, A.K.; Priyadarshi, N.; Azam, F.; Padmanaban, S.; Bhoi, A.K. A comprehensive study on electrical vehicle in charging infrastructure, challenges and future scope. In *Electric Vehicles: Modern Technologies and Trends*; Springer: Singapore, 2021; pp. 271–285.
5. Khan, M.A.; Ahmed, A.; Husain, I.; Sozer, Y.; Badawy, M. Performance analysis of bidirectional DC–DC converters for electric vehicles. *IEEE Trans. Ind. Appl.* **2015**, *51*, 3442–3452. [CrossRef]
6. Rodríguez-Benítez, O.M.; Ponce-Silva, M.; Aquí-Tapia, J.A.; Claudio-Sánchez, A.; Vela-Váldes, L.G.; Lozoya-Ponce, R.E.; Cortés-García, C. Comparative performance and assessment study of a current-fed DC-DC resonant converter combining Si, SiC, and GaN-based power semiconductor devices. *Electronics* **2020**, *9*, 1982. [CrossRef]
7. Dobakhshari, S.S.; Milimonfared, J.; Taheri, M.; Moradisizkoohi, H. A quasi-resonant current-fed converter with minimum switching losses. *IEEE Trans. Power Electron.* **2016**, *32*, 353–362. [CrossRef]
8. Sha, D.; You, F.; Wang, X. A high-efficiency current-fed semi-dual-active bridge DC–DC converter for low input voltage applications. *IEEE Trans. Ind. Electron.* **2015**, *63*, 2155–2164. [CrossRef]
9. Pan, X.; Li, H.; Liu, Y.; Zhao, T.; Ju, C.; Rathore, A.K. An overview and comprehensive comparative evaluation of current-fed-isolated-bidirectional DC/DC converter. *IEEE Trans. Power Electron.* **2019**, *35*, 2737–2763. [CrossRef]
10. Sree, K.R.; Rathore, A.K.; Breaz, E.; Gao, F. Soft-switching non-isolated current-fed inverter for PV/fuel cell applications. *IEEE Trans. Ind. Appl.* **2015**, *52*, 351–359. [CrossRef]
11. Samanta, S.; Rathore, A.K. Wireless power transfer technology using full-bridge current-fed topology for medium power applications. *IET Power Electron.* **2016**, *9*, 1903–1913. [CrossRef]
12. Kosenko, R.; Husev, O.; Chub, A. Full soft-switching high step-up current-fed DC-DC converters with reduced conduction losses. In Proceedings of the 2015 IEEE 5th International Conference on Power Engineering, Energy and Electrical Drives (POWERENG), Riga, Latvia, 11–13 May 2015; IEEE: Piscataway, NJ, USA, 2015; pp. 170–175.
13. Jin, L.; Liu, B.; Duan, S. ZVS soft switching operation range analysis of three-level dual-active bridge DC–DC converter under phase shift control strategy. *IEEE Trans. Ind. Appl.* **2018**, *55*, 1963–1972. [CrossRef]
14. Xu, X.; Bishop, M.; Oikarinen, D.G.; Hao, C. Application and modeling of battery energy storage in power systems. *CSEE J. Power Energy Syst.* **2016**, *2*, 82–90. [CrossRef]
15. Zhang, Z.; Xie, S.; Shang, X.; Qian, Q.; Xu, J. Modeling and controller optimization for current-fed isolated bidirectional DC–DC converters. *J. Power Electron.* **2020**, *20*, 1592–1603. [CrossRef]
16. Guo, Z.; Sun, K.; Wu, T.F.; Li, C. An improved modulation scheme of current-fed bidirectional DC–DC converters for loss reduction. *IEEE Trans. Power Electron.* **2017**, *33*, 4441–4457. [CrossRef]
17. Kondrath, N. Bidirectional DC-DC converter topologies and control strategies for interfacing energy storage systems in microgrids: An overview. In Proceedings of the 2017 IEEE International Conference on Smart Energy Grid Engineering (SEGE), Oshawa, ON, Canada, 14–17 August 2017; IEEE: Piscataway, NJ, USA, 2017; pp. 341–345.
18. Zhu, L.; Bai, H.; Brown, A.; Keuck, L. A Current-fed Three-port DC/DC Converter for Integration of On-board Charger and Auxiliary Power Module in Electric Vehicles. In Proceedings of the 2021 IEEE Applied Power Electronics Conference and Exposition (APEC), Phoenix, AZ, USA, 14–17 June 2021; IEEE: Piscataway, NJ, USA, 2021; pp. 577–582.
19. Weinert, T.; Oberschelp, W.; Schroder, G. A current-fed DC/DC converter for the efficient charging of HV capacitors in mobile applications. In Proceedings of the 2016 18th European Conference on Power Electronics and Applications (EPE'16 ECCE Europe), Karlsruhe, Germany, 5–9 September 2016; IEEE: Piscataway, NJ, USA, 2016; pp. 1–10.
20. Shi, Y.; Li, R.; Xue, Y.; Li, H. Optimized operation of current-fed dual active bridge DC–DC converter for PV applications. *IEEE Trans. Ind. Electron.* **2015**, *62*, 6986–6995. [CrossRef]
21. Kumar, N.; Panda, S.K. A multipurpose and power quality improved electric vessels charging station for the seaports. *IEEE Trans. Ind. Inform.* **2022**, *19*, 3254–3261. [CrossRef]
22. Kumar, N.; Panda, S.K. Smart High Power Charging Networks and Optimal Control Mechanism for Electric Ships. *IEEE Trans. Ind. Inform.* **2022**, *19*, 1476–1483. [CrossRef]
23. Siu, J.Y.; Kumar, N.; Panda, S.K. Attack detection and mitigation using multi-agent system in the deregulated market. In Proceedings of the 2021 IEEE 12th Energy Conversion Congress & Exposition-Asia (ECCE-Asia), Singapore, 24–27 May 2021; pp. 821–826.

24. Siu, J.Y.; Kumar, N.; Panda, S.K. Command Authentication Using Multi-agent System for Attacks on the Economic Dispatch Problem. *IEEE Trans. Ind. Appl.* **2022**, *58*, 4381–4393. [CrossRef]
25. Pragaspathy, S.; Rao, R.R.; Karthikeyan, V.; Bhukya, R.; Nalli, P.K.; Korlepara, K.P. Analysis and appropriate choice of power converters for electric vehicle charging infrastructure. In Proceedings of the 2022 2nd International Conference on Artificial Intelligence and Smart Energy (ICAIS), Coimbatore, India, 23–25 February 2022; pp. 1554–1558.
26. Akhtar, M.F.; Raihan, S.R.; Rahim, N.A.; Akhtar, M.N.; Bakar, E.A. Recent Developments in DC-DC Converter Topologies for Light Electric Vehicle Charging: A Critical Review. *Appl. Sci.* **2023**, *13*, 1676. [CrossRef]
27. Zheng, Y.; Li, S.; Smedley, K.M. Non-isolated high step-down converter with ZVS and low current ripples. *IEEE Trans. Ind. Electron.* **2018**, *66*, 1068–1079. [CrossRef]
28. Liu, Z.; Lin, X.; Gao, Y.; Xu, R.; Wang, J.; Wang, Y.; Liu, J. Fixed-time sliding mode control for DC/DC buck converters with mismatched uncertainties. *IEEE Trans. Circuits Syst. I Regul. Pap.* **2022**, *70*, 472–480. [CrossRef]
29. Shen, X.; Liu, J.; Liu, Z.; Gao, Y.; Leon, J.I.; Vazquez, S.; Wu, L.; Franquelo, L.G. Sliding Mode Control of Neutral-Point-Clamped Power Converters with Gain Adaptation. *IEEE Trans. Power Electron.* **2024**, *39*, 9189–9201. [CrossRef]
30. Sharma, P.; Palwalia, D.K.; Sharma, A.K.; Priyadarshi, N.; Padmanaban, S. Coati optimized FOPID controller for non-isolated DC–DC converters in EV charging application. *IET Power Electron.* **2024**. [CrossRef]
31. Pramanik, R.; Pati, B.B. Modelling and control of a non-isolated half-bridge bidirectional DC-DC converter with an energy management topology applicable with EV/HEV. *J. King Saud Univ.-Eng. Sci.* **2023**, *35*, 116–122. [CrossRef]
32. Wu, Y.E.; Tai, C.H. Novel Bidirectional Isolated DC/DC Converter with High Gain Ratio and Wide Input Voltage for Electric Vehicle Storage Systems. *Batteries* **2022**, *8*, 240. [CrossRef]
33. Park, H.P.; Kim, M.; Jung, J.H. Bidirectional current-fed CLLC resonant converter employing asymmetric PWM. *IEEE Trans. Energy Convers.* **2021**, *36*, 3167–3177. [CrossRef]
34. Tomar, P.S.; Srivastava, M.; Verma, A.K. An Improved Current-Fed Bidirectional DC–DC Converter for Reconfigurable Split Battery in EVs. *IEEE Trans. Ind. Appl.* **2020**, *56*, 6957–6967. [CrossRef]
35. Wu, F.; Fan, S.; Luo, S. Elimination of Transient Current Mutation and Voltage Spike for Buck–Boost Current-Fed Isolated DC–DC Converter. *IEEE Trans. Ind. Electron.* **2020**, *68*, 10928–10937. [CrossRef]
36. Piasecki, S.; Zaleski, J.; Jasinski, M.; Bachman, S.; Turzyński, M. Analysis of AC/DC/DC Converter Modules for Direct Current Fast-Charging Applications. *Energies* **2021**, *14*, 6369. [CrossRef]
37. Liu, Y.; Chen, C.; Chen, K.; Syu, Y.; Dung, N.A. High-Frequency and High-Efficiency Isolated Two-Stage Bidirectional DC–DC Converter for Residential Energy Storage Systems. *IEEE J. Emerg. Sel. Top. Power Electron.* **2020**, *8*, 1994–2004. [CrossRef]
38. Sharma, A.K.; Vyas, A.; Sharma, P. Comparative study of DC-DC converter with different control techniques. In Proceedings of the Recent Advances in Renewable Energy Sources—RARES2021, Engineering College, Banswara, India, 26–27 February 2021.
39. Kang, T.; Kim, C.; Suh, Y.; Park, H.; Kang, B.; Kim, D. A design and control of bi-directional non-isolated DC-DC converter for rapid electric vehicle charging system. In Proceedings of the 2012 Twenty-Seventh Annual IEEE Applied Power Electronics Conference and Exposition (APEC), Orlando, FL, USA, 5–9 February 2012; pp. 14–21.
40. Rahman, M.M.; Uddin, M.N.; Islam, M.K. Performance enhancement of a bi-directional DC-DC converter using a Ćuk converter for electric vehicle applications. In Proceedings of the 2015 IEEE 28th Canadian Conference on Electrical and Computer Engineering (CCECE), Halifax, NS, Canada, 3–6 May 2015; pp. 875–880.
41. Tandon, S.; Rathore, A.K.; Narasimharaju, B.L. A ZVS series resonant current-fed PWM controlled DC-DC converter. In Proceedings of the 2020 IEEE Transportation Electrification Conference & Expo (ITEC), Chicago, IL, USA, 23–26 June 2020; pp. 320–325.
42. Malek, H.; Dadras, S.; Yin, C.; Chen, Y.Q. Fractional order proportional-resonant controller. In Proceedings of the 2018 Annual American Control Conference (ACC), Milwaukee, WI, USA, 27–29 June 2018; IEEE: Piscataway, NJ, USA, 2018; pp. 3086–3091.
43. Wu, Y.E.; Ke, Y.T. A novel bidirectional isolated DC-DC converter with high voltage gain and wide input voltage. *IEEE Trans. Power Electron.* **2020**, *36*, 7973–7985. [CrossRef]
44. Packnezhad, M.; Farzanehfard, H. Soft-switching high step-up/down converter using coupled inductors with minimum number of components. *IEEE Trans. Ind. Electron.* **2020**, *68*, 7938–7945. [CrossRef]
45. Mohammadi, M.R.; Amoorezaei, A.; Khajehoddin, S.A.; Moez, K. A high step-up/step-down LVS-parallel HVS-series ZVS bidirectional converter with coupled inductors. *IEEE Trans. Power Electron.* **2021**, *37*, 1945–1961.
46. Shu, L.; Chen, W.; Shi, M.; Liu, R.; Gao, S.; Deng, F. Improved Control Strategy of Triple-Voltage Three-Phase DAB (T 2-DAB) Converter for Current Stress and Zero-Voltage-Switching Optimization. *IEEE J. Emerg. Sel. Top. Power Electron.* **2021**, *10*, 773–784. [CrossRef]
47. Cúnico, L.M.; Alves, Z.M.; Kirsten, A.L. Efficiency-optimized modulation scheme for three-phase dual-active-bridge DC–DC converter. *IEEE Trans. Ind. Electron.* **2020**, *68*, 5955–5965. [CrossRef]